energies

MDPI

Article

Development of a 1D Finite-Volume Model for the Simulation of Solid Oxide Fuel Cells

Alberto Cammarata *, Paolo Colbertaldo and Stefano Campanari

Department of Energy, Politecnico di Milano, Via Lambruschini 4, 20156 Milano, Italy; paolo.colbertaldo@polimi.it (P.C.); stefano.campanari@polimi.it (S.C.)
* Correspondence: alberto.cammarata@polimi.it

Abstract

This work presents the development and validation of a 1D finite-volume model for the simulation of planar solid oxide cells (SOCs), developed for integration in more complex systems and process simulations. The model allows to investigate the temperature, composition, and current density profiles along the channel. In this work, the Fick's equations typically used to calculate the concentration overpotential due to H_2 and H_2O diffusion in the electrode are improved compared to 1D SOC models available in the literature. In particular, the approximate analytical solution of the dusty gas model (DGM) equations allows for a better definition of H_2 and H_2O mixture diffusion coefficients, which are relevant, for instance, in the case of solid oxide fuel cells (SOFCs) fed with reformate gas mixtures. Differently from other 1D models available in the literature, the model developed is validated using experimental SOFC polarization curves covering a wide range of operating conditions in terms of molar fraction of H_2 (21–93%) and H_2O (7–50%) in the fuel, temperature (550–750 °C), and fuel utilization factor (exceeding 90%), demonstrating that 1D SOC models retain a good description of the physical processes occurring within the cell. While this work focuses on a co-flow SOFC configuration, the model can simulate a counter-flow configuration and electrolysis operation without modifying the model equations.

Keywords: solid oxide fuel cell; 1D SOFC model; channel-level model; finite-volume model

1. Introduction

Solid oxide fuel cells (SOFCs) and solid oxide electrolysis cells (SOECs) are emerging energy conversion technologies that can support the energy transition. Their use can improve the efficiency of the existing energy conversion concepts, like in the case of an SOFC used for cogeneration applications, or prompt the development of new concepts, like multi-energy systems based on reversible solid oxide cells (rSOCs) [1] or hybrid power generation systems integrating an SOFC with gas or steam cycles [2]. Modern SOCs can operate at an intermediate temperature range between 600 and 800 °C thanks to the fabrication of very thin electrolytes (10 µm or lower), which are typically made of yttria-stabilized zirconia (YSZ), or thanks to the use of alternative electrolyte materials (e.g., scandia stabilized zirconia). On the one hand, the high temperatures bring several advantages compared to similar electrochemical devices based on polymeric or alkaline electrolytes, including higher efficiency, the possibility of thermal integration at system level, fuel flexibility, and absence of expensive catalysts. On the other hand, the main

Academic Editor: JongHoon Kim

Received: 1 January 2026
Revised: 2 February 2026
Accepted: 13 February 2026
Published: 15 February 2026

drawbacks include a faster degradation of the main cell components and the need to carefully manage internal thermal gradients.

Using accurate models to predict the performance of SOFC (or SOEC) is a crucial aspect for the development of energy systems based on this technology. The model dimensionality and complexity can vary substantially, including 1D approaches developed along the main direction of the gas flows [3], 1D + 1D or 2D models with a refined description of the processes occurring within the electrodes [4] and at the cell layer boundaries, and 3D models of the solid oxide cell (or stack) using commercial software like COMSOL Multiphysics® [5] and CFD (computational fluiddynamics) approach. The review work of Wu et al. [6] provides an in-depth description of the available SOFC models, highlighting strengths, weaknesses, and field of application for each of them. In particular, 1D models can be more easily integrated into wider system simulations due to the significant computational burden of 2D and 3D models, allowing the system optimization while retaining a good description of physical processes occurring within the stack. Two- and three-dimensional models provide additional insights on the stack internal operating conditions and can improve the performance estimation, especially at high current density [7].

This paper presents an updated version of a stationary 1D finite-volume model for the simulation of planar SOFCs and SOECs, which has already been validated and used in several works [3,8] and which can be used both in co-flow and counter-flow configurations. Differently from previous versions, the model is developed to allow running within Aspen Plus® for wider system and process simulations; the Aspen environment provides built-in functions for the calculation of physical and thermodynamic properties of gases and facilitates the model integration.

Focusing on stationary 1D models describing the SOFC internal conditions along the channel direction, either in a co-flow or counter-flow arrangement, the state-of-the-art modelling approach and equations used are substantially unchanged compared to the first models of this kind developed about 20 years ago (e.g., [3,9]). A typical 1D SOFC model solves the species mass balances to find the fuel and oxidant composition along the channel length, energy balances for the temperature distribution, and an electrochemical model using local partial pressures and temperature to calculate the local current density produced by the cell, assuming that the cell voltage is fixed.

The energy balance equations can present some variations depending on the assumptions made. While the temperature profiles of the fuel and air streams are always calculated, the solid parts (electrodes, electrolyte, and interconnects) can be assumed to be at the same temperature at each axial coordinate [10]. Alternatively, a finer grid allows to distinguish the temperature of the PEN (positive-electrolyte-negative), which is the assembly including the electrodes and the electrolyte, from the interconnect temperature [11]. The interconnects at the fuel and air sides can also be separated for an improved description, which is the approach followed in this work. The interconnects might also be internally divided into smaller pieces, depending on the assumed geometry, which was reported to provide an improved level of detail in the cross-flow configuration [3]. While the axial heat conduction in the solid parts is always considered, this term is typically neglected in the gas phase, which is also an assumption made in this work, since the thermal conductivity of gases is 10–100 times lower compared to that of solid materials (especially the interconnect). In addition, the radiative heat transfer between PEN and interconnects, which is typically considered in other works, is replaced by an equivalent heat conduction term, as also done by Jie et al. [12].

Regarding the electrochemical model, a voltage balance involving the ideal Nernst voltage, the imposed cell voltage, and the overpotentials is solved to find the local current density. Since electrochemical reactions are always assumed to occur at the electrode–

electrolyte interface, the ohmic loss due to the ionic current only occurs in the electrolyte bulk, while the electronic ohmic loss can be considered for the electrodes and the interconnects. However, the latter contribution is typically neglected due to the high conductivity of the interconnect materials. In this work, the electronic ohmic loss in the electrodes is also neglected due to its very low contribution. Indeed, assuming to calculate ionic and electronic conductivities with the relations used in several references [3,11–13] and assuming a very thin electrolyte of 3 μm, a 1000 μm fuel electrode (conservatively thick, since typical fuel-electrode supported SOCs employ <400–500 μm electrodes), and a 50 μm air electrode, the area specific resistances at 700 °C would be equal to 3.554 Ω mm^2, 0.033 Ω mm^2, and 0.004 Ω mm^2, for the electrolyte, fuel, and air electrodes respectively, which justifies the exclusion of electronic losses from the model. Activation losses are always calculated using Butler–Volmer equations, either in their complete form, as done in this work, or using a simplified version valid in the low or high overpotential region.

Concentration overpotentials at the fuel side are typically more important compared to the air side, both due to the fuel electrode-supported architecture of modern SOFCs and the high fuel utilization factor targeted in real applications. In 1D SOC models, a simplified Fick approach is always used to estimate the species partial pressures at the electrode–electrolyte interface, since solving the rigorous dusty gas model (DGM) equations along the electrode thickness would require a 2D approach. One of the aims of this paper is to clarify the derivation of Fick's equations for H_2 and H_2O diffusion in the electrode, starting from the complete DGM equations, as some confusion is still present in the literature. For instance, most authors assume that the total pressure along the electrode thickness is constant, which can either introduce an approximation in the model developed [10,14,15], or it can justify the replacement of partial pressures in the Fick's equations with molar fractions [12,16]. While the latter situation would not introduce errors, the molar fractions calculated in this way are not consistent by themselves, as their sum can exceed one in some conditions (while still providing a correct estimation of the concentration loss), as demonstrated in this work. Moreover, the molecular diffusion coefficient of H_2 and H_2O in a multi-component gas mixture, which can be a relevant parameter for SOFCs operating with natural gas or in the co-electrolysis of H_2O and CO_2, is typically calculated with a generic relation [3,17] that can be derived from Stefan–Maxwell equations, assuming that each component diffuses in a stagnant gas mixture [18]. However, this is not the case for the fuel electrode, where equimolar counter-diffusion of H_2 and H_2O occurs. In this work, an improved molecular diffusion coefficient for multi-component mixtures is defined based on the approximate analytical solution of DGM equations [12].

Another gap existing in the literature is the validation of 1D SOC models over a wide range of operating conditions, as their simplicity might limit their applicability in a narrow range of operating conditions near the calibration point. The model developed in this work is calibrated and validated using experimental polarization curves of an SOFC, covering a wide range of operating conditions in terms of H_2 and H_2O molar fraction in the fuel, temperature, and fuel utilization factor (exceeding 90%). The experimental data are reported in ref. [4], which also includes a numerical investigation using a 1D + 1D model integrating the DGM for species diffusion in the electrode, coupled with a distributed electrochemical model applied throughout the electrode thickness. One of the aims of this work is to demonstrate that the same set of data can be accurately described by a simpler 1D model over a wide range of operating conditions.

2. Model Description

The model developed is designed for the simulation of standard solid oxide cells using Y-doped zirconia as electrolyte. The electrochemical reactions (1) and (2), representing the hydrogen oxidation reaction (HOR) and the oxygen reduction reaction (ORR), occur at the fuel and air electrode, respectively. In fuel cell mode, H_2 is oxidized to H_2O, consuming an oxygen ion in the electrolyte and producing two electrons in the electronic conducting phase (e.g., nickel). Electrons flow through an external resistance towards the positive electrode (air electrode), where they combine with oxygen to produce an oxygen ion in the electrolyte. The HOR and the ORR proceed forward and backward in fuel cell and electrolysis mode, respectively.

$$H_2 + O^{2-} \leftrightarrow H_2O + 2e^- \quad (1)$$

$$\frac{1}{2}O_2 + 2e^- \leftrightarrow O^{2-} \quad (2)$$

Figure 1 (left) shows a generic solid oxide cell stack made of multiple planar cells stacked on top of each other, each cell containing several gas channels as the one shown on the right-hand side of Figure 1. The model developed in this work considers a single channel as geometric domain, assuming that the whole stack (or cell) can be represented by a number of identical channels, which significantly limits model complexity. The developed finite-volume model is one-dimensional in the direction of the channel; it assumes steady-state operation, with either co-flow or counter-flow arrangement (the co-flow configuration is shown in the figure for simplicity), and it can be used to model both fuel cell and electrolyzer modes. The model is implemented in Aspen Plus® (Aspen Technology, Inc., Bedford, MA, USA) environment, which allows exploiting a built-in equations solver and accurate datasets for the calculation of thermodynamic and physical properties of gas mixtures.

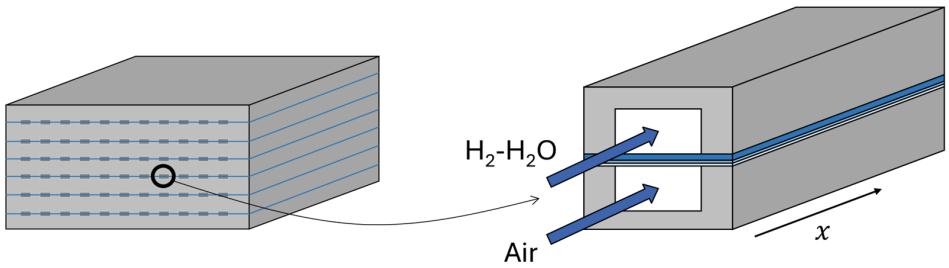

Figure 1. (**Left**) solid oxide cell stack made by several cells. (**Right**) single channel within a solid oxide cell. The model developed in this work considers a single channel as the geometrical domain.

The model inputs are the channel geometry, the conditions of the inlet streams (temperature, composition, pressure, and molar flow rate), several parameters required to model the physical processes, and the cell voltage, which is assumed to be constant throughout the channel (electrode equipotential assumption). The main outputs of the 1D model are the distribution along the axial direction of:

- The composition (x_i) and temperatures (T_f and T_a) of the gas streams;
- The temperature of the PEN structure (T_{PEN});
- The temperature of the interconnect at the fuel side and air side ($T_{int,f}$ and $T_{int,a}$);
- The current density ($i_{O^{2-}}$) and the electrochemical overpotentials (η_k).

Figure 2 shows the main dimensions defining the channel geometry, and Table 1 defines some relevant geometrical parameters, where ε_{fe} and ε_{ae} are the porosities of the fuel and air electrode, respectively.

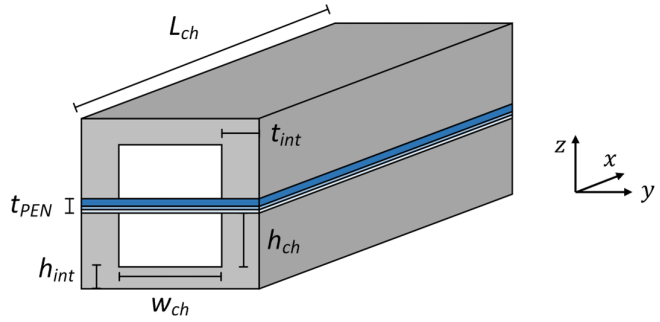

Figure 2. Main geometrical dimensions of the SOFC channel.

Table 1. Relevant geometrical parameters derived from the input channel geometry.

Symbol	Equation	Description
l_{act}	$w_{ch} + 2 \cdot t_{int}$	Active area per unit length
t_{PEN}	$t_{fe} + t_{ae} + t_{ely}$	PEN thickness
A_{int}	$l_{act} \cdot h_{int} + 2 \cdot t_{int} \cdot h_{ch}$	Cross-sectional area of the interconnect
A_{fe}	$l_{act} \cdot t_{fe} \cdot \left(1 - \varepsilon_{fe}\right)$	Cross-sectional area of the fuel electrode
A_{ae}	$l_{act} \cdot t_{ae} \cdot \left(1 - \varepsilon_{ae}\right)$	Cross-sectional area of the air electrode
A_{ely}	$l_{act} \cdot t_{ely}$	Cross-sectional area of the electrolyte
A_{PEN}	$A_{fe} + A_{ae} + A_{ely}$	Cross-sectional area of the PEN assembly

The finite-volume solution algorithm includes the division of the channel in N small pieces as the one shown in Figure 3 (left), which will be called control volume (CV). Assuming that the cell voltage is fixed throughout the channel, the electrochemical model allows to calculate the local current density $i_{O^{2-}}$, which is equal to the small (but finite) current (ΔI) flowing through the interconnects of the CV divided by the active area contained in it (ΔA_{act}), as shown in Equation (3).

$$i_{O^{2-}} = \frac{\Delta I}{\Delta A_{act}} = \frac{\Delta I}{l_{act} \cdot \Delta x} \tag{3}$$

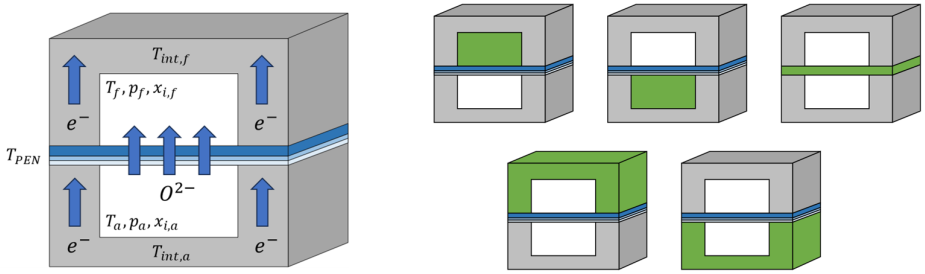

Figure 3. The channel is divided into N control volumes (**left**). Each control volume is further divided into 5 sub-volumes (**right**). The current density is calculated for each control volume, while the energy balances are solved for all $5 \times N$ sub-volumes. Mass balances are solved for the $2 \times N$ sub-volumes enclosing the fuel and air streams.

The electrochemical model is zero-dimensional, meaning that electrochemical reactions are assumed to only occur at the interface between the electrode and the bulk of the electrolyte. Coherently with the use of YSZ as electrolyte, short-circuit electronic currents in the electrolyte are neglected, hence the current collected by the interconnects is equal to the ionic current flowing in the electrolyte.

As shown in Figure 3 (right), each CV is further divided into 5 sub-volumes enclosing the fuel and air channels, the interconnects, and the PEN structure. Mass and energy

balances are solved for each of these $5 \times N$ sub-volumes to find the temperature and gas composition along the channel. A uniform temperature is defined for the solid parts (interconnects and PEN sub-volumes) of each CV, resulting in $3 \times N$ unknown temperatures. The fuel and air temperatures at the outlet interface of each CV are also unknown, resulting in $5 \times N$ unknown temperatures in total, which is equal to the number of energy balance equations.

Axial heat conduction in the x direction is considered for the PEN and the interconnects, while it is neglected for gas streams due to the low thermal conductivity of the gases. In the y direction, only the convective heat exchange between gases and interconnects is considered (with exchange area per unit length equal to $4 \cdot h_{ch}$). The heat exchange in the z direction includes the convective heat transfer between gases and solid parts, the conductive heat transfer between PEN and interconnects, and the heat loss, which is assumed to be uniformly distributed on the external interconnect surfaces. The radiative heat exchange between PEN and interconnects is neglected since the temperature of the solid parts is always found to be very similar in the z and y directions even when radiative heat exchange is not considered, while the view factors are very small in the x direction.

The main equation used for the calculation of the local current density is the voltage balance shown in Equation (4). The cell voltage (V_{cell}) is fixed (if the total current is fixed, instead of the voltage, the same model can be run iteratively to find the voltage which matches the required current), and E_{H_2} is the ideal maximum (minimum) cell voltage in fuel cell (electrolysis) mode. The term $E^0_{H_2}$ depends on temperature, and a simple correlation can be derived by fitting thermodynamic data [3]. The partial pressures of hydrogen and steam (p_{H_2} and p_{H_2O}) used in Equation (5) are those found locally in the fuel channel; similarly, the local oxygen partial pressure in the air channel (p_{O_2}) is used. The overpotentials, η_k, shift the cell voltage from the ideal value, decreasing its performance. In the model developed, both the overpotentials and the current density are positive in fuel cell mode and negative in electrolysis mode. All the overpotentials depend on the current density, and Equation (4) is used to implicitly calculate $i_{O^{2-}}$.

$$V_{cell} = E_{H_2} - \eta_{conc} - \eta_{ohm} - \eta_{act} - \eta_{leakage} \tag{4}$$

$$E_{H_2} = E^0_{H_2} + \frac{R \cdot T_{PEN}}{2 \cdot F} ln\left(\frac{p_{H_2} \cdot p^{1/2}_{O_2}}{p_{H_2O}}\right) \tag{5}$$

Equation (6) is used to calculate $\eta_{leakage}$, which accounts for the fact that the measured open-circuit voltage (OCV) is typically slightly lower compared to the ideal value calculated with Equation (5), even if the external current is null [4,19]; since it is difficult to identify and model the phenomena behind this mismatch, which might be due to gas leaks or a short-circuit electronic current within the electrolyte, $\eta_{leakage}$ should only be seen as a small numerical correction to better fit experimental data. In fuel cell (or electrolysis) mode, the maximum current density i_{max} is calculated assuming that all the equivalent hydrogen (or steam) is consumed, generating a corresponding faradaic current. Therefore, the leakage loss is important near the OCV and tends to zero when the current density is large (in absolute value).

$$\eta_{leakage} = (E_{H_2} - OCV) \cdot \left(1 - \frac{i_{O^{2-}}}{i_{max}}\right) \tag{6}$$

The concentration overpotential, which is calculated with Equation (7), accounts for the fact that the ideal voltage should be calculated using the species partial pressures in the proximity of the reaction site (i.e., $p_{H_2,r}$, $p_{H_2O,r}$, and $p_{O_2,r}$), which is assumed to be located at the electrode–electrolyte interface.

$$\eta_{conc} = \frac{R \cdot T_{PEN}}{2 \cdot F} ln\left(\frac{p_{H_2}}{p_{H_2,r}} \cdot \frac{p_{H_2O,r}}{p_{H_2O}} \cdot \frac{p_{O_2}^{1/2}}{p_{O_2,r}^{1/2}}\right) \tag{7}$$

The partial pressures of H_2, H_2O, and O_2 at the electrode–electrolyte interfaces are calculated using Equations (8)–(10), in line with most literature works on 1D SOFC models [11,15]. The coefficient l_{act}/w_{ch} is included to account for the fact that the reference surface for the diffusion process is lower than the active area. The calculation of the diffusion coefficients in the porous electrodes $D_{i,p}$ can vary among different works, with some approaches even assuming that $D_{H_2,p}$ and $D_{H_2O,p}$ are equal [14,15]. The coefficients $D_{i,p}$ are typically calculated as a combination of the Knudsen diffusion coefficient ($D^e_{K,i}$) and the molecular diffusion coefficient in the gas mixture ($D^e_{i,mix}$) of each species, as shown in Equation (15).

$$p_{H_2,r} = p_{H_2} - \frac{i_{O^{2-}} \cdot R \cdot T_{PEN} \cdot t_{fe}}{2 \cdot F \cdot D_{H_2,p}} \cdot \frac{l_{act}}{w_{ch}} \tag{8}$$

$$p_{H_2O,r} = p_{H_2O} + \frac{i_{O^{2-}} \cdot R \cdot T_{PEN} \cdot t_{fe}}{2 \cdot F \cdot D_{H_2O,p}} \cdot \frac{l_{act}}{w_{ch}} \tag{9}$$

$$p_{O_2,r} = p_{ch} - (p_{ch} - p_{O_2}) \cdot exp\left(\frac{i_{O^{2-}} \cdot R \cdot T_{PEN} \cdot t_{ae}}{4 \cdot F \cdot p_{ch} \cdot D_{O_2,p}} \cdot \frac{l_{act}}{w_{ch}}\right) \tag{10}$$

In this work, the binary diffusion coefficients $D_{i,j}$ are calculated according to the Fuller method, which is valid for pressures below 35 bar [20], and it is widely adopted in other similar works [12,21]. The effective molecular diffusion coefficients $D^e_{i,j}$ can be found multiplying the binary diffusion coefficients by ε/τ. The effective Knudsen diffusion coefficient $D^e_{K,i}$ is calculated with Equation (14), where r_p is the average pore radius, and MM_i is the molar mass of species i.

Since the concentration overpotential due to O_2 diffusion is typically small, and the cathodic gas mixture is often a N_2-O_2 binary mixture, $D^e_{O_2,mix}$ is calculated using a generic literature model, represented by Equation (13), which can be derived from Stefan–Maxwell equations assuming that a species diffuses in a stagnant gas mixture [18] (which is not the case for the fuel electrode where equimolar counter-diffusion of H_2 and H_2O occurs). Instead of using a relation similar to Equation (13), as done in other works [3,17], the molecular diffusion coefficients of H_2 and H_2O in the gas mixture are calculated with Equations (11) and (12), according to the approximate solution of the DGM equations shown in the Appendix A. In particular, the Appendix A shows the derivation of Equations (8) and (9) and the coefficients $D^e_{H_2,mix}$, $D^e_{H_2O,mix}$, $D_{H_2,p}$, and $D_{H_2O,p}$, starting from the rigorous DGM equations. In particular, it is demonstrated that defining $D^e_{H_2,mix}$ and $D^e_{H_2O,mix}$, as done in Equations (11) and (12), allows to achieve results very similar to the DGM solution in a multi-component gas mixture compared to using a generic correlation as Equation (13).

$$\frac{1}{D^e_{H_2,mix}} = \sum_{j \neq H_2}^{NS} \frac{x_j}{D^e_{H_2,j}} + \frac{x_{H_2}}{D^e_{H_2,H_2O}} \tag{11}$$

$$\frac{1}{D^e_{H_2O,mix}} = \sum_{j \neq H_2O}^{NS} \frac{x_j}{D^e_{H_2O,j}} + \frac{x_{H_2O}}{D^e_{H_2,H_2O}} \tag{12}$$

$$\frac{1}{D^e_{O_2,mix}} = \frac{1}{(1 - x_{O_2})} \cdot \sum_{j \neq O_2}^{NS} \frac{x_j}{D^e_{O_2,j}} \tag{13}$$

$$D^e_{K,i} = \frac{\varepsilon}{\tau} \cdot \frac{2}{3} \cdot r_p \cdot \sqrt{\frac{8 \cdot R \cdot T_{PEN}}{\pi \cdot MM_i}} \tag{14}$$

$$\frac{1}{D_{i,p}} = \frac{1}{D^e_{K,i}} + \frac{1}{D^e_{i,mix}} \tag{15}$$

The ohmic loss is calculated with Equation (16), where the main contribution is due to the oxygen ion conductivity (σ) along the electrolyte thickness (t_{ely}), and $r_{contact}$ is a calibration parameter that can be used to fit the data, representing an additional electric contact resistance, which includes the effect of the interconnects (material electric resistance and contact resistance) and other contributions that are not (or cannot be) explicitly considered in the model.

$$\eta_{ohm} = i_{O^{2-}} \cdot \left(\frac{t_{ely}}{\sigma} + r_{contact} \right) \tag{16}$$

$$\sigma = \frac{\sigma_0}{T_{PEN}} \cdot exp\left(-\frac{E_{act,\sigma}}{R \cdot T_{PEN}} \right) \tag{17}$$

The activation overpotentials in the fuel electrode ($\eta_{act,fe}$) and air electrode ($\eta_{act,ae}$) are calculated using Butler–Volmer Equations (18) and (20), and their sum is equal to the overall activation overpotential (η_{act}). The form of the Butler–Volmer equations is taken from ref. [4], and both k_{HOR} and k_{ORR} are referred to the active area of the cell. The coefficients α_{fe} and α_{ae} are the charge-transfer coefficients of the HOR and ORR.

$$i_{O^{2-}} = i_{0,fe} \cdot \left[exp\left(\alpha_{fe} \frac{2 \cdot F \cdot \eta_{act,fe}}{R \cdot T_{PEN}} \right) - exp\left(-\left(1 - \alpha_{fe}\right) \frac{2 \cdot F \cdot \eta_{act,fe}}{R \cdot T_{PEN}} \right) \right] \tag{18}$$

$$i_{0,fe} = k_{HOR} \cdot p^a_{H_2,r} \cdot p^b_{H_2O,r} \cdot exp\left(-\frac{E_{act,fe}}{R \cdot T_{PEN}} \right) \tag{19}$$

$$i_{O^{2-}} = i_{0,ae} \cdot \left[exp\left(\alpha_{ae} \frac{2 \cdot F \cdot \eta_{act,ae}}{R \cdot T_{PEN}} \right) - exp\left(-(1 - \alpha_{ae}) \frac{2 \cdot F \cdot \eta_{act,ae}}{R \cdot T_{PEN}} \right) \right] \tag{20}$$

$$i_{0,ae} = k_{ORR} \cdot p^c_{O_2,r} \cdot exp\left(-\frac{E_{act,ae}}{R \cdot T_{PEN}} \right) \tag{21}$$

The mass balance equation for each species i can be written in differential form, as shown in Equation (22), accounting for NR possible chemical or electrochemical reactions and the stoichiometric coefficient ν_{ij} of species i in reaction j. The reaction rate r_j (mol s^{-1} m^{-2}) is specific to the active area of the cell. The sum of the HOR and the ORR can be considered as a single overall reaction whose reaction rate is calculated as in Equation (23), with stoichiometric coefficients equal to −1, 1, and −0.5 for H_2, H_2O, and O_2, respectively.

Concerning water gas shift (WGS) and methane steam reforming (MSR) reactions, a global reaction approach is used, as described by Equations (24) and (25). The forward kinetic constant for the WGS reaction is calculated using the parameters derived by Wang et al. [22]. Since the pre-exponential factor given in the reference is equal to 0.0183 mol s^{-1} m^{-3} Pa^{-2}, and it is specific to the electrode volume, this value is multiplied by $101{,}325^2$ and by an assumed electrode thickness equal to 250 μm, which is a purposely low thickness for fuel-electrode-supported cells, in order to be conservative. Therefore, γ_{WGS} is equal to 46,970 mol s^{-1} m^{-2}, it is specific to the active area, and it requires partial pressure expressed in atmospheres. The activation energy $E_{act,WGS}$ is equal to 103.8 kJ mol^{-1}.

Regarding the MSR reaction, which is of interest mostly for fuel cell operation, the kinetic model reported by Timmermann et al. is selected [23]. This model is valid in the range of 600–750 °C, which is in line with the operating temperature of modern SOFCs; the

temperature at cell outlet might be even larger, but methane is typically consumed near the inlet section of the cell. The pre-exponential factor appearing in the kinetic constant k_f^{MSR}, which is equal to 1483 mol s^{-1} m^{-2} in the original reference, is scaled by a factor 1.73 to refer to the active area instead of the surface touched by the gas. The scaling factor is derived from the channel width (w_{ch}) and interconnect thickness (t_{int}) stated in ref. [23], equal to 1.5 mm and 0.55 mm, respectively. Therefore, γ_{MSR} and $E_{act,MSR}$ are equal to 856 mol s^{-1} m^{-2} and 61 kJ mol^{-1}. Note that all the equilibrium and kinetic constants are calculated using the local PEN temperature.

$$\frac{1}{l_{act}}\frac{d\dot{n}_i}{dx} = \sum_j^{NR} r_j \cdot \nu_{ij} \tag{22}$$

$$r_{HOR+ORR} = \frac{i_{O^{2-}}}{2 \cdot F} \tag{23}$$

$$r_{WGS} = k_f^{WGS} \cdot p_{CO} \cdot p_{H_2O} \cdot \left(1 - \frac{p_{H_2} \cdot p_{CO_2}}{K_{eq}^{WGS} \cdot p_{CO} \cdot p_{H_2O}}\right) \tag{24}$$

$$r_{MSR} = k_f^{MSR} \cdot p_{CH_4} \cdot \left(1 - \frac{p_{H_2}^3 \cdot p_{CO}}{K_{eq}^{MSR} \cdot p_{CH_4} \cdot p_{H_2O}}\right) \tag{25}$$

$$k_f^{WGS} = \gamma_{WGS} \cdot exp\left(-\frac{E_{act,WGS}}{R \cdot T_{PEN}}\right) \tag{26}$$

$$k_f^{MSR} = \gamma_{MSR} \cdot exp\left(-\frac{E_{act,MSR}}{R \cdot T_{PEN}}\right) \tag{27}$$

Equations (28)–(32) represent the energy balances for the fuel channel, air channel, PEN assembly, fuel-side interconnect, and air-side interconnect, respectively. The energy exchanges between gas and solid parts are further detailed in Table 2. The left-hand side of Equations (28) and (29) represents the variation in enthalpy flow along the axial coordinate, where $\dot{n}_f$ and $\dot{n}_a$ are the overall molar flow rate at the fuel and air side, respectively, and the specific enthalpy, which is calculated using Peng–Robinson correlations imported from Aspen Plus®, is a function of the local gas composition and temperature. The left-hand side of Equations (30)–(32) accounts for the axial conduction of the solid parts. A heat loss term q_{loss}, expressed in W m^{-2}, is also included in Equations (31) and (32), and it is specific to the interconnects surfaces facing adjacent cells. All other external surfaces of the channel are assumed to be adiabatic.

$$\frac{d\left(\dot{n}_f \cdot h_f\right)}{dx} = \dot{Q}_{f-PEN} + \dot{H}_{f-PEN} + \dot{Q}_{f-int_f} \tag{28}$$

$$\frac{d\left(\dot{n}_a \cdot h_a\right)}{dx} = \dot{Q}_{a-PEN} + \dot{H}_{a-PEN} + \dot{Q}_{a-int_a} \tag{29}$$

$$A_{PEN} \cdot k_{PEN} \cdot \frac{d^2 T_{PEN}}{dx^2} = \dot{Q}_{f-PEN} + \dot{Q}_{a-PEN} + \dot{Q}_{PEN-int_f} + \dot{Q}_{PEN-int_a} + \dot{H}_{f-PEN} + \dot{H}_{a-PEN} + l_{act} \cdot i_{O^{2-}} \cdot V_{cell} \tag{30}$$

$$A_{int} \cdot k_{int} \cdot \frac{d^2 T_{int_f}}{dx^2} = \dot{Q}_{f-int_f} - \dot{Q}_{PEN-int_f} + q_{loss} \cdot l_{act} \tag{31}$$

$$A_{int} \cdot k_{int} \cdot \frac{d^2 T_{int_a}}{dx^2} = \dot{Q}_{a-int_a} - \dot{Q}_{PEN-int_a} + q_{loss} \cdot l_{act} \tag{32}$$

Table 2. Summary of heat and enthalpy exchanges between gas and solid parts.

	PEN	Interconnect (Fuel and/or Air Side)
Gas Channel (Fuel or Air)	$\dot{Q}_{gas-PEN} = h_{conv} \cdot w_{ch} \cdot (1-\varepsilon) \cdot (T_{PEN} - T_{gas})$ $\dot{H}_{gas-PEN} = \sum_{i}^{NS} \frac{d\dot{n}_i}{dx} \cdot h_i$ [1]	$\dot{Q}_{gas-int} = h_{conv} \cdot (w_{ch} + 2 \cdot h_{ch}) \cdot (T_{int} - T_{gas})$
PEN	-	$\dot{Q}_{PEN-int} = 2 \cdot \frac{k_{int}}{h_{ch}} \cdot t_{int} \cdot (1-\varepsilon) \cdot (T_{PEN} - T_{int})$

[1] h_i is the enthalpy of the pure species i calculated with the local PEN or gas temperature in case $\frac{d\dot{n}_i}{dx}$ is positive or negative, respectively.

The local convective heat transfer coefficients (h_{conv}) for the fuel and air streams are calculated from the local Nusselt number, the gas thermal conductivity, and the hydraulic diameter (d_h) of the channels. The local Nusselt number is calculated using Equation (33) [24], where the Graetz number is calculated with Equation (34), x is the distance from the channel entrance, Re is the Reynolds number, and Pr is the Prandtl number. The Nusselt number rapidly declines from the channel entry reaching an asymptotic value equal to Nu_∞, representative of a fully developed laminar flow. The asymptotic Nusselt number, which is only a function of the channel aspect ratio, is calculated with the relation provided in ref. [24], and it is equal to 3–5 for aspect ratios (w_{ch}/h_{ch}) in the range 1–4.

$$Nu = Nu_\infty + 8.9336 \cdot \left(\frac{1000}{Gz}\right)^{-0.5386} exp\left(-\frac{6.7275}{Gz}\right) \quad (33)$$

$$Gz = Re \cdot Pr \cdot \frac{d_h}{x} \quad (34)$$

The PEN thermal conductivity is calculated as shown in Equation (35).

$$k_{PEN} = \frac{k_{fe} \cdot A_{fe} + k_{ae} \cdot A_{ae} + k_{ely} \cdot A_{ely}}{A_{PEN}} \quad (35)$$

3. Results and Discussion

3.1. Model Calibration and Validation

The experimental data on commercial 5 × 5 cm^2 (4 × 4 cm^2 active area) cells, reported by Neri et al. [4], are used to validate the model. The cell is manufactured by Elcogen (Tallinn, Estonia) and is composed by a thick Ni-YSZ composite electrode (400 µm), a thin YSZ electrolyte (1.5 µm), a GDC ($Ce_{0.9}Gd_{0.1}O_{2-\delta}$) barrier layer (1.6 µm), and a LSC ($La_{0.6}Sr_{0.4}CoO_{3-\delta}$) single-phase cathode (15 µm). The experimental polarization curves used for the model validation refer to fuel cell operation and cover a wide range of operating conditions:

- 7% humidified fuel gas mixtures with 21–93% H_2 fraction and N_2 balance at 750 °C;
- 50% H_2 fuel gas mixtures with 10–50% steam content and N_2 balance at 750 °C;
- 7% humidified fuel gas mixture with 93% H_2 fraction at 550–700 °C.

A large excess of air (assumed composition is 21% O_2 and 79% N_2) is always used at the air-electrode side of the cell, and the co-flow configuration is selected. Note that the limiting current density is approached when the H_2 fraction is low, allowing to evaluate the model performance at large fuel utilization factors typical of real applications. More detailed information on the cells, the experimental setup, and the experimental procedures are available in ref. [4].

Since the cell used as reference for the experimental data was tested in a furnace with a fixed setpoint temperature, the temperature distribution is assumed uniform throughout the

channel length for all gas and solid parts. As demonstrated by Neri et al. [4], this hypothesis can be justified by the inconsistent numerical results stemmed from the assumption of adiabaticity, and the large thermal conductivity of the nickel current collector, which efficiently dissipates the heat produced by electrochemical reactions.

Table 3 summarizes the main parameters used for model validation. Most of the values are derived from ref. [4], while several parameters are calibrated. The ohmic parameters σ_0 and $E_{act,\sigma}$ are calibrated from EIS data shown in ref. [4]; note that the contact resistance grew significantly as a consequence of a blackout (15 min) when passing from experiments at low temperature to 750 °C; therefore, two values of σ_0 are calculated (the blackout only affected the ohmic resistance of the cell). The remaining eight parameters are calibrated using the polarization curves and include the activation loss parameters, the anode tortuosity, and the inlet fuel flow rate. Note that there is uncertainty about the fuel flow rate that actually reaches the cell due to leakages on the fuel pathway and in the fuel distributor (the experimental setup avoids sealings, which may damage the cells during disassembling), which justifies its inclusion in the set of calibrated variables. The calibrated inlet fuel flow rate is equal to 5.486 Nml min^{-1} cm^{-2}, which is similar to the 6.25 Nml min^{-1} cm^{-2} value indicated in ref. [4].

Table 3. Input parameters used for the model validation.

Parameter	Value	Source
Channel		
L_{ch}	4 cm	[4]
w_{ch}	2 mm	[4]
h_{ch}	2 mm	[4]
t_{int}	1 mm	[4]
h_{int}	1 mm	[4]
$A_{act,tot}$	$L_{ch} \cdot l_{act} = 1.6$ cm^2	
$\dot{n}_{f,in}$	5.486 Nml min^{-1} cm^{-2}	Fitted
$\dot{n}_{a,in}$	93.75 Nml min^{-1} cm^{-2}	[4]
N	100	
Fuel Electrode		
t_{fe}	400 µm	[4]
ε_{fe}	0.28	[4]
τ_{fe}	7.5	Fitted
$r_{p,fe}$	0.16 µm	[4]
$E_{act,fe}$	100 kJ mol^{-1}	Fitted
k_{HOR}	3.2×10^8 A m^{-2}	Fitted
a	0.5	Fitted
b	−1	Fitted
α_{fe}	0.5	[4]
Air Electrode		
t_{ae}	15 µm	[4]
ε_{ae}	0.2	[4]
τ_{ae}	3.0	[4]
$r_{p,ae}$	0.25 µm	[4]
$E_{act,ae}$	135.0 kJ mol^{-1}	Fitted
k_{ORR}	2.2×10^{11} A m^{-2}	Fitted
c	0.22	[4]
α_{ae}	0.65	[4]
Electrolyte		
t_{ely}	3.1 µm	[4]
$E_{act,\sigma}$	61.1 kJ mol^{-1}	Fitted from EIS [4]
σ_0 [1]	261,945 S K m^{-1}	Fitted from EIS [4]
$r_{contact}$	0.0	

[1] This value is valid for experiments with varying p_{H_2} and p_{H_2O} performed at 750 °C. For experiments at 700 °C, 650 °C, 600 °C, and 550 °C, σ_0 = 464,167 S K m^{-1}.

Figure 4 shows the experimental polarization curves and the model predictions for different H_2 and H_2O concentrations (Figure 4a,b), and different temperatures (Figure 4c). At each cell voltage, the average current density is calculated with Equation (36).

$$i_{av} = \frac{1}{L_{ch}} \cdot \int_0^{L_{ch}} i_{O^{2-}} dx \tag{36}$$

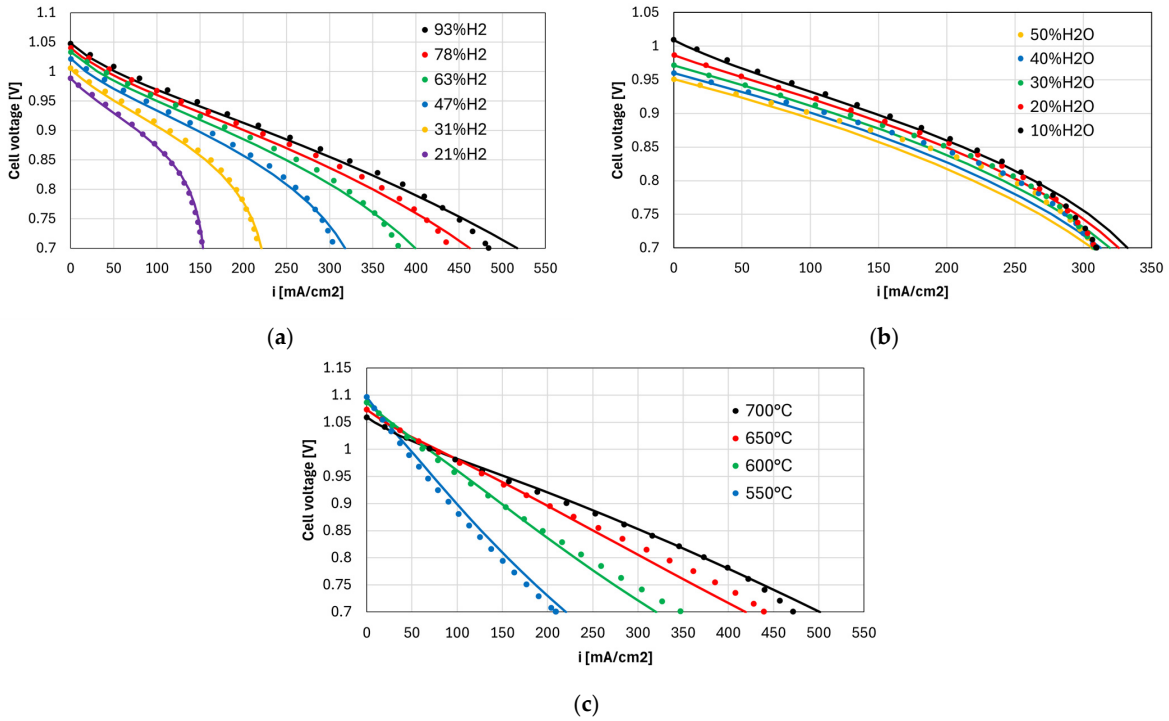

Figure 4. Experimental polarization curves (dots) and model predictions (lines) at different operating conditions: (**a**) 7% H_2O and 21–93% H_2 (N_2 balance) at 750 °C, (**b**) 50% H_2 and 10–50% H_2O (N_2 balance) at 750 °C, (**c**) 7% humidified H_2 at 550–700 °C.

Considering the wide range of operating conditions investigated in terms of reactants concentrations, temperature, and fuel utilization, the good matching between model and experiments demonstrates the generality of the model developed. Notably, the model accuracy is not significantly worse compared to the results shown in ref. [4], where the same set of data is described using a 1D + 1D model, which couples the dusty gas model with a distributed electrochemical model along the electrode thickness for a better representation of ohmic and activation overpotentials.

The measured OCV is always 6–24 mV lower compared to the theoretical value E_{H_2}. Therefore, the leakage loss calculated with Equation (6) is limited. The limiting current is approached for the case with 21% H_2, as 95.6% of the available hydrogen is consumed near 0.7 V. Notably, the model correctly predicts the cell performance also in this extreme case, where concentration losses play a major role.

Figure 5 shows the average overpotentials, calculated using Equation (37), in different selected operating conditions. Since the overpotentials represent the exergy lost per unit charge (J C^{-1}), they are weighted by the local current produced. Note that the oxygen concentration loss is negligible in all cases, and the anode concentration loss includes contributions from both H_2O and H_2 diffusion processes in the electrode.

$$\eta_{k,av} = \frac{1}{i_{av} \cdot L_{ch}} \cdot \int_0^{L_{ch}} i_{O^{2-}} \cdot \eta_k \cdot dx \tag{37}$$

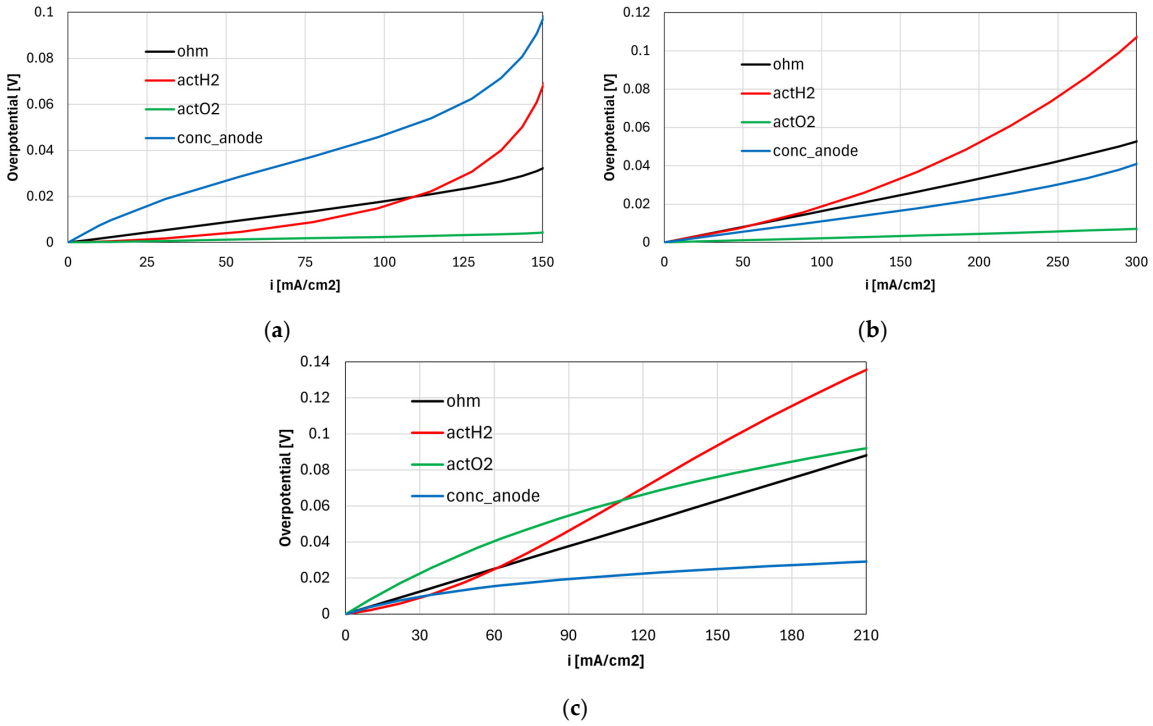

Figure 5. Polarization losses calculated in selected operating conditions: (**a**) 7% H_2O and 21% H_2 (N_2 balance) at 750 °C, (**b**) 50% H_2 and 50% H_2O at 750 °C, (**c**) 7% humidified H_2 at 550 °C.

Figure 5a shows the overpotentials for the case with 7% H_2O and 21% H_2 (N_2 balance) at 750 °C and suggests that the concentration loss always dictates the cell performance. Most of the anode concentration loss is due to steam diffusion in the low current density region since its concentration in the channel is low compared to hydrogen. In other words, if p_{H_2O} or p_{H_2} in the channel are low, $p_{H_2O,r}$ or $p_{H_2,r}$ can be very different from their channel values percentage-wise, significantly increasing the concentration polarization (see Equations (7)–(9)). The H_2 concentration polarization becomes dominant only above 125 mA cm^{-2} due to the fuel depletion, and it grows exponentially at larger current densities. Since the calibrated H_2 exponent (coefficient a in Table 3) is equal to 0.5, the anode activation loss grows significantly at large current densities.

Figure 5b shows the overpotentials calculated for the case with 50% H_2 and 50% H_2O at 750 °C. Concentration losses are limited due to the large channel concentration of both H_2 and H_2O. Hydrogen and steam diffusion processes contribute approximately equally to the anode concentration loss, since p_{H_2O} is large even at low current densities, and the H_2 utilization factor is limited in the high current region (78% at 0.7 V). Anode activation and ohmic overpotentials have the greatest impact on the cell performance.

Figure 5c shows the polarization losses for the case with 93% H_2 and 7% H_2O at 550 °C. The concentration overpotential gives the smallest contribution to the cell polarization due to the relatively weak dependence of diffusion processes on temperature. Contrarily, the cathode activation overpotential grows significantly, being the most important contributor together with the anode activation loss.

Each calibration parameter has a different impact on the simulation results depending on the operating conditions. For instance, since concentration losses dictate the cell polarization for the case with 21% H_2 at low current densities, the anode tortuosity is primarily calibrated by matching the model results with the experimental points in this region. The inlet fuel flow rate is calibrated using the same curve near the limiting current region.

Since concentration overpotentials are higher in conditions where either H_2 or H_2O are low, fuel mixtures without nitrogen have low concentration losses and higher activation losses. In particular, the polarization curves of the H_2-H_2O mixtures (with null or low N_2) at 750 °C are used to calibrate k_{HOR}, a, and b. As a general consideration, the performance at high current densities, which is dominated by the anodic activation overpotential (see Figure 5b), tends to decrease more rapidly compared to the model predictions, which is particularly visible in Figure 4b. Therefore, the H_2O exponent (b) is fixed to -1, which is assumed to be a lower bound. Similarly, the H_2 exponent (a) is fixed to 0.5. Higher values of the hydrogen exponent would excessively increase the performance of the curves with a large H_2 fraction. The activation energies $E_{act,fe}$, $E_{act,ae}$, and the pre-exponential factor k_{ORR} are calibrated using the polarization curves at low temperatures (Figure 4c) where the temperature effect related to the activation energies is present, and the cathode activation overpotential is more relevant.

In general, the trends discussed and the overpotentials calculated are similar to those shown in ref. [4], suggesting that both models can be used for the simulation of solid oxide fuel cells.

3.2. Adiabatic Model with Reformate Fuel

In order to test the adiabatic model (which also includes energy balances) in a condition representative of a real application, the operating conditions calculated in ref. [2] are considered. In particular, Table 4 shows the operating conditions of an SOFC integrated in a hybrid power generation system that also includes a bottoming steam cycle. A co-flow configuration is assumed for the simulation.

Table 4. Operating conditions of the SOFC in the hybrid system with a bottoming steam cycle [2].

Parameter	Value	Description
General		
V_{cell} [1]	0.8 V	Cell voltage
U_f	66.4%	Single-pass H_2 utilization factor
Heat loss	2%	Heat loss (fraction of fuel LHV)
T_{out}	800 °C	Outlet cell temperature
Fuel Inlet		
$T_{f,in}$	521 °C	Inlet fuel temperature
$p_{f,in}$	1.15 bar	Inlet fuel pressure
x_{H_2}	24.16%	Inlet H_2 fraction
x_{H_2O}	32.83%	Inlet H_2O fraction
x_{CO}	4.45%	Inlet CO fraction
x_{CO_2}	26.66%	Inlet CO_2 fraction
x_{CH_4}	11.55%	Inlet CH_4 fraction
x_{N_2}	0.35%	Inlet N_2 fraction
Air Inlet		
$T_{a,in}$	754 °C	Inlet air temperature
$p_{a,in}$	1.15 bar	Inlet air pressure
x_{O_2}	20.73%	Inlet O_2 fraction
x_{N_2}	77.28%	Inlet N_2 fraction
x_{H_2O}	1.03%	Inlet H_2O fraction
x_{Ar}	0.96%	Inlet Ar fraction

[1] Reference [2] shows 0.86 V, but this value is too large to guarantee a significant current density near the channel exit.

The global heat loss assumption is used to calculate q_{loss} (see Equations (31) and (32)), which is equal to 40 W m^{-2}. The investigated operating conditions are peculiar because of the low inlet fuel temperature equal to 521 °C, which might cause significant thermal

gradients near the SOFC entrance. All parameters shown in Table 3 are used for the simulation, with some exceptions:

- The fuel and air mass flow rates at channel inlet are derived to match the fuel utilization factor and the outlet cell temperature stated in Table 4.
- The channel length is set to 9 cm, which is a value in line with applicative cells, and the channel width is fixed to 3 mm for the same reason.
- The parameter σ_0 is fixed to 464,167 S K m^{-1} (used for the simulations in Figure 4c).

The thermal conductivity of the anode, cathode, and electrolyte (k_{fe}, k_{ae}, k_{ely}) is fixed to 2 W m^{-1} K^{-1}, while the interconnect conductivity (k_{int}) is equal to 20 W m^{-1} K^{-1}.

Figure 6 shows the results of the adiabatic simulation. Figure 6a shows the temperature profiles calculated for the PEN, interconnects, and gas streams. Although the fuel inlet temperature is equal to 521 °C, the minimum value of the temperature axis is fixed to 720 °C for clarity.

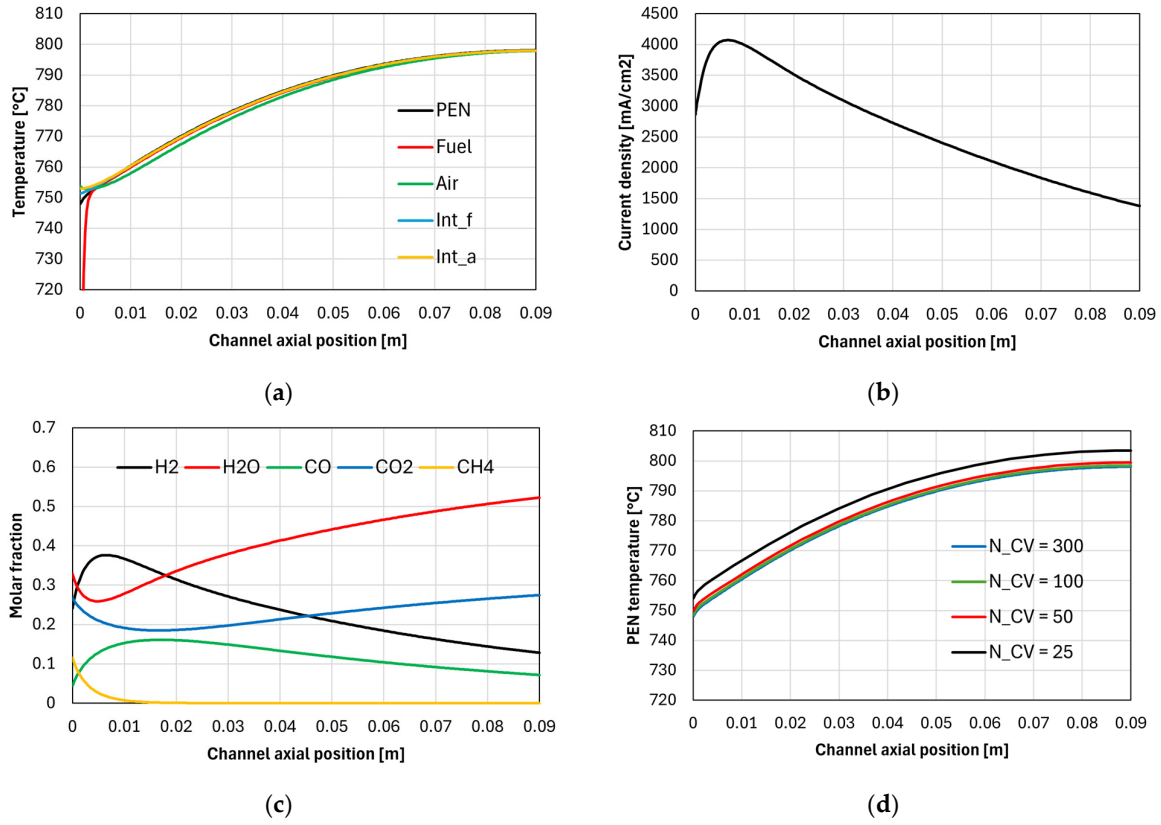

Figure 6. Results of the adiabatic simulation: (**a**) temperature distribution of PEN, interconnects, and gas streams, (**b**) current density profile, (**c**) fuel stream composition along the channel, (**d**) effect of grid refinement on PEN temperature distribution.

The fuel reaches a temperature close to that of the air stream almost instantly, which is due to its relatively low thermal inertia (the inlet air molar flow rate is 5.42 times larger). The PEN temperature near the channel inlet seems to be the only one slightly affected by the low fuel temperature; this is attributed to its relatively large resistance to axial conduction, since the temperature of the fuel interconnect is higher despite having a larger contact surface with the fuel stream. The PEN temperature remains large due to the heat exchange with the air stream and the interconnects, but there is a very small region where the PEN temperature gradient reaches 3 °C mm^{-1}, which is larger compared to the value calculated in the middle of the channel, equal to 0.5 °C mm^{-1}.

The fact that the model used for the kinetics of MSR is derived in the 600–750 °C temperature range [23] might seem in contrast with the fact that the fuel enters at 521 °C and exists at about 800 °C. However, since the PEN temperature is used to calculate the MSR reaction rate, which is expected to better reflect reality, and considering that CH_4 is almost completely consumed after 1 cm, the MSR reaction is expected to occur between 748 °C and 760 °C, which is very close to the upper bound of the model validity, equal 750 °C. From the data shown in ref. [23], the kinetic constant k_f^{MSR} calculated in this work at 760 °C is only about 5% larger compared to the real value.

Figure 6b shows that the current density reaches a maximum value near the channel entrance, which corresponds to the H_2 concentration peak shown in Figure 6c. After this point, the current density decreases due to H_2 depletion and H_2O formation, despite the increasing temperature trend. Figure 6c shows that methane is rapidly consumed producing H_2, overcompensating the H_2 consumed by electrochemical reactions up to the peak already mentioned. The existence of a H_2 concentration peak near the channel inlet is typical of SOFCs operating with reformate, as also demonstrated in other modelling works [3,8].

Figure 6d shows the effect of grid refinement on the PEN temperature distribution. Since the PEN temperature frequently appears both in the electrochemical, chemical, and energy balance models, it is considered representative of the status of all other calculated variables. Figure 6d shows that the PEN temperature profiles calculated with 100 and 300 control volumes almost perfectly overlap, suggesting that dividing the channel into 100 control volumes is sufficient to achieve the grid independence.

Overall, the model developed correctly simulates the most relevant physical processes occurring within a SOFC, elucidating the internal operating conditions like the temperature, current density, and gas composition profiles.

It shall be noted that the model is also flexible by the point of view of the cell operating mode, since its extension to the case of counter-flow configuration is straightforward; in the counter-flow case, the inlet conditions assigned for the air stream (temperature, pressure, composition, and molar inlet flow rate) are imposed at $x = L_{ch}$ instead of $x = 0$, and a negative inlet air molar flow rate must be assigned. The model calculates a distribution of negative air flow rates throughout the channel, and further model modifications are not necessary. Similarly, simulating the electrolysis configuration does not require any mathematical modification; in this case, the cell voltage assigned must be larger than the Nernst voltage, resulting in a distribution of negative current densities calculated by the electrochemical model.

4. Conclusions

This work presented the development and validation of a 1D finite-volume model for the simulation of planar SOCs. The model is developed to facilitate the introduction of SOCs in wider energy or industrial system models and process simulations in Aspen Plus®, which provides built-in functions for the calculation of physical and thermodynamic properties of gases. The model allows to simulate the most relevant physical processes occurring within an SOC and to investigate its internal operating conditions in terms of temperature, current density, and gas composition profiles.

Differently from other works, the H_2 and H_2O molecular diffusion coefficients in the gas mixture, which are used to calculate the overall diffusion coefficients in the porous electrode, are derived from an approximated analytical solution of the DGM equations, resulting in a better accuracy of the Fick model. Moreover, the model is calibrated and validated using experimental SOFC polarization curves covering a wide range of operating conditions in terms of H_2 and H_2O molar fraction in the fuel, temperature, and fuel

utilization factor. A good matching between model results and experimental data is achieved in all conditions with a single set of calibrated parameters, demonstrating that 1D models can accurately describe the most relevant physical processes occurring in the cell, despite their relative simplicity compared to multi-dimensional approaches. Although the results presented in this work focus on a co-flow SOFC configuration, the counter-flow arrangement and the case of electrolysis operation can be simulated without further modifications to the model.

Author Contributions: Conceptualization, A.C., P.C. and S.C.; methodology, software, validation, formal analysis, data curation, writing—original draft preparation, visualization, A.C.; investigation, writing—review and editing, A.C., P.C. and S.C.; supervision, project administration, resources, P.C. and S.C. All authors have read and agreed to the published version of the manuscript.

Funding: This research received no external funding.

Data Availability Statement: Data is contained within the article.

Conflicts of Interest: The authors declare no conflicts of interest.

Abbreviations

CFD	computational fluid dynamics
CV	control volume
DGM	dusty gas model
EIS	electrochemical impedance spectroscopy
HOR	hydrogen oxidation reaction
MSR	methane steam reforming
OCV	open circuit voltage
ORR	oxygen reduction reaction
PEN	positive-electrolyte-negative
SOC	solid oxide cell
SOEC	solid oxide electrolysis cell
SOFC	solid oxide fuel cell
WGS	water gas shift
YSZ	yttria-stabilized zirconia

Appendix A

Calculation of H_2 and H_2O Partial Pressure at Cell Reaction Site

Estimating the quantity of reacting species reaching the cell reaction sites is one of the key steps in the solid oxide cell model; in particular, the partial pressures of hydrogen and steam directly influence the concentration overpotential (Equation (7)) and the activation overpotential (Equation (19)).

The most referenced approach to evaluate the variation in partial pressure from the bulk region of the cell channels to the actual reaction sites, due to the diffusion process in the porous electrode structure, is the dusty gas model (DGM).

Diffusion of each species, i, through the porous electrode according to the DGM can be expressed by Equation (A1). In Equation (A1), the term J_i is the species molar flux (mol m^{-2} s^{-1}), and B is the electrode permeability; both molecular and Knudsen diffusion coefficients are intended as effective coefficients, meaning that they are already multiplied by ε/τ.

$$\sum_{j \neq i} \frac{x_j \cdot J_i - x_i \cdot J_j}{D^e_{i,j}} + \frac{J_i}{D^e_{K,i}} = -\frac{1}{R \cdot T} \cdot \left(\frac{dp_i}{dz} + \frac{x_i \cdot p \cdot B}{D^e_{K,i} \cdot \mu} \cdot \frac{dp}{dz} \right) \quad \text{(A1)}$$

This set of equations cannot be solved analytically in its complete form. Assuming equimolar counter-diffusion ($J_{H_2O} = -J_{H_2}$) and neglecting the term including the electrode permeability, it is possible to derive Equations (A2) and (A3):

$$J_{H_2}\left(\sum_{j\neq H_2}^{NS}\frac{x_j}{D^e_{H_2,j}} + \frac{x_{H_2}}{D^e_{H_2,H_2O}} + \frac{1}{D^e_{K,H_2}}\right) = J_{H_2}\left(\frac{1}{D^e_{H_2,mix}} + \frac{1}{D^e_{K,H_2}}\right) = -\frac{1}{R\cdot T}\cdot\frac{dp_{H_2}}{dz} \tag{A2}$$

$$J_{H_2}\left(\sum_{j\neq H_2O}^{NS}\frac{x_j}{D^e_{H_2O,j}} + \frac{x_{H_2O}}{D^e_{H_2,H_2O}} + \frac{1}{D^e_{K,H_2O}}\right) = J_{H_2}\left(\frac{1}{D^e_{H_2O,mix}} + \frac{1}{D^e_{K,H_2O}}\right) = \frac{1}{R\cdot T}\cdot\frac{dp_{H_2O}}{dz} \tag{A3}$$

Assuming that the term in the parenthesis is constant, which is always true for a H_2-H_2O mixture since $D^e_{H_2,mix} = D^e_{H_2O,mix} = D^e_{H_2,H_2O}$, but it introduces an additional error for multi-component mixtures (in this case, the channel composition can be used to calculate $D^e_{H_2,mix}$ and $D^e_{H_2O,mix}$), the integration along the fuel electrode thickness (z direction) then gives Equations (A4) and (A5), where the molar fluxes are expressed in terms of current density.

$$p_{H_2,r} = p_{H_2} - \frac{i_{O^{2-}}\cdot R\cdot T\cdot t_{fe}}{2\cdot F\cdot D_{H_2,p}}\cdot\frac{l_{act}}{w_{ch}} \tag{A4}$$

$$p_{H_2O,r} = p_{H_2O} + \frac{i_{O^{2-}}\cdot R\cdot T\cdot t_{fe}}{2\cdot F\cdot D_{H_2O,p}}\cdot\frac{l_{act}}{w_{ch}} \tag{A5}$$

Some authors use Equations (A6) and (A7) instead of Equations (A4) and (A5), which is equivalent to assuming that the pressure throughout the electrode is constant and equal to the channel pressure (p_{ch}). Although using Equations (A4) and (A5) or Equations (A6) and (A7) to calculate concentration overpotentials gives the same results, calculating molar fractions in the reaction site with Equations (A6) and (A7) gives inconsistent results, as demonstrated below.

$$x_{H_2,r} = x_{H_2} - \frac{i_{O^{2-}}\cdot R\cdot T\cdot t_{fe}}{2\cdot F\cdot D_{H_2,p}\cdot p_{ch}}\cdot\frac{l_{act}}{w_{ch}} \tag{A6}$$

$$x_{H_2O,r} = x_{H_2O} + \frac{i_{O^{2-}}\cdot R\cdot T\cdot t_{fe}}{2\cdot F\cdot D_{H_2O,p}\cdot p_{ch}}\cdot\frac{l_{act}}{w_{ch}} \tag{A7}$$

Figure A1 shows $x_{H_2,r}$, $x_{H_2O,r}$, $p_{H_2,r}$, and $p_{H_2O,r}$ calculated with the rigorous DGM and with the Fick's model (Equations (A4)–(A7), assuming $\frac{l_{act}}{w_{ch}}$ equal to 1) for different H_2 molar fractions in the fuel (balance H_2O). Since atmospheric pressure (1.01 bar) is assumed in the channel, molar fractions and partial pressures are almost the same in the Fick's model. The current density is always assumed equal to 1000 mA cm^{-2}, which is a purposely large value in order to highlight the differences between the DGM and the Fick model. The fuel electrode parameters shown in Table 3 are used for the calculations. The permeability, B, is equal to 7.84×10^{-17} m^2, which is estimated based on the electrode porosity, tortuosity, and particle diameter (assumed equal to 1 μm) [25]. The temperature is assumed equal to 750 °C.

Figure A1 shows that the molar fractions estimated with Equations (A6) and (A7) (represented by the triangles in the figure) are by themselves inconsistent since their sum exceeds 1 in all conditions. Moreover, there is a significant difference compared to the values calculated with the DGM. The H_2 and H_2O partial pressures calculated with the Fick model are in very good agreement with the DGM, as shown in Figure A1. Since the coefficient B is assumed to be null to derive the analytical solution represented by the Fick equations, the Fick model (Equations (A4) and (A5)) and the DGM are in good agreement because the permeability coefficient is actually very low. Note that the total pressure

calculated in the reaction site is always equal to about 1.27 bar, which is significantly larger compared to the channel value (atmospheric pressure).

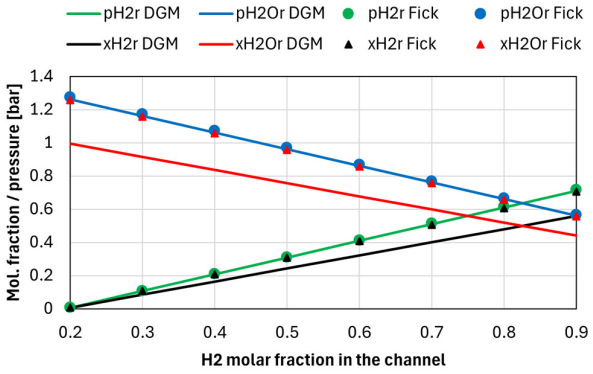

Figure A1. Molar fractions and partial pressures in the reaction site estimated using the DGM and the Fick's model for different H_2 fractions in the channel (H_2O balance). The current density is assumed equal to 1000 mA cm^{-2}, and the temperature is equal to 750 °C.

Figure A2 shows the partial pressures of H_2 and H_2O calculated with the DGM and the Fick model along the electrode thickness, assuming different channel compositions and current densities. The chosen gas compositions are those calculated at channel inlet and outlet in the adiabatic simulation performed in this work (see Figure 6). In general, there is very good agreement between the DGM and the Fick model. The largest discrepancy is found at the electrode end (Figure A2a), where the steam partial pressure calculated with the Fick model is 2% larger compared to the DGM. The same calculations have been performed using an equation similar to Equation (13) to calculate $D^e_{H_2,mix}$ and $D^e_{H_2O,mix}$ (instead of using Equations (11) and (12)), as done in other works, finding errors up to 8%.

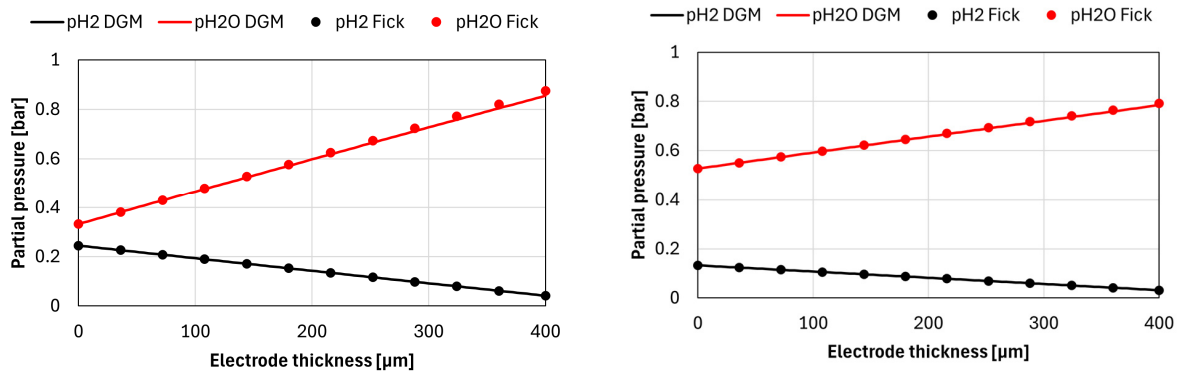

Figure A2. Partial pressures of H_2 and H_2O calculated within the electrode using the DGM and the Fick model for different channel compositions and current densities at 750 °C: (**a**) 24.16% H_2, 32.83% H_2O, 4.45% CO, 26.66% CO_2, and 11.55% CH_4 at 1000 mA cm^{-2}; (**b**) 13.12% H_2, 51.94% H_2O, 7.32% CO, and 27.34% CO_2 at 500 mA cm^{-2}.

References

1. Ficili, M.; Colbertaldo, P.; Campanari, S.; Guandalini, G. Investigating the Partial Load of Reversible Solid Oxide Cell Systems: A Focus on Balance of Plant and Thermal Integration. *Appl. Energy* **2025**, *391*, 125876. [CrossRef]
2. Campanari, S.; Mastropasqua, L.; Gazzani, M.; Chiesa, P.; Romano, M.C. Predicting the Ultimate Potential of Natural Gas SOFC Power Cycles with CO_2 Capture—Part A: Methodology and Reference Cases. *J. Power Sources* **2016**, *324*, 598–614. [CrossRef]
3. Campanari, S.; Iora, P. Comparison of Finite Volume SOFC Models for the Simulation of a Planar Cell Geometry. *Fuel Cells* **2005**, *5*, 34–51. [CrossRef]

4. Neri, J.; Cammarata, A.; Donazzi, A. Experimental and Model Investigation of a Solid Oxide Fuel Cell Operated Under Low Fuel Flow Rate. *J. Electrochem. Soc.* **2023**, *170*, 124506. [CrossRef]
5. Razbani, O.; Assadi, M.; Andersson, M. Three Dimensional CFD Modeling and Experimental Validation of an Electrolyte Supported Solid Oxide Fuel Cell Fed with Methane-Free Biogas. *Int. J. Hydrogen Energy* **2013**, *38*, 10068–10080. [CrossRef]
6. Wu, Z.; Zhu, P.; Huang, Y.; Yao, J.; Yang, F.; Zhang, Z.; Ni, M. A Comprehensive Review of Modeling of Solid Oxide Fuel Cells: From Large Systems to Fine Electrodes. *Chem. Rev.* **2025**, *125*, 2184–2268. [CrossRef]
7. Koksharov, A.; Jahnke, T. 3D Modelling of Electrolyzer and Fuel Cells with NEOPARD-X Framework: Dimensionality Effects. In Proceedings of the European Fuel Cells and Hydrogen Conference, Capri, Italy, 17–19 September 2025.
8. Spallina, V.; Mastropasqua, L.; Iora, P.; Romano, M.C.; Campanari, S. Assessment of Finite Volume Modeling Approaches for Intermediate Temperature Solid Oxide Fuel Cells Working with CO-Rich Syngas Fuels. *Int. J. Hydrogen Energy* **2015**, *40*, 15012–15031. [CrossRef]
9. Aguiar, P.; Adjiman, C.S.; Brandon, N.P. Anode-Supported Intermediate Temperature Direct Internal Reforming Solid Oxide Fuel Cell. I: Model-Based Steady-State Performance. *J. Power Sources* **2004**, *138*, 120–136. [CrossRef]
10. Zhang, B.; Farida, N.; Zhou, N.; Oryshchyn, D.; Colon-rodriguez, J.J.; Shadle, L.; Bayham, S.; Tucker, D. A Real-Time Distributed Solid Oxide Electrolysis Cell (SOEC) Model for Cyber-Physical Simulation. *Appl. Energy* **2025**, *388*, 125607. [CrossRef]
11. Xia, L.; Hua, Q.; Ni, S. Modelica Based Modelling and Thermodynamic Analysis of Co-Flow and Counter-Flow Solid Oxide Fuel Cell System. *Energy Convers. Manag.* **2024**, *317*, 118839. [CrossRef]
12. Jie, H.; Liao, J.; Zhu, G.; Hong, W. Nonlinear Model Predictive Control of Direct Internal Reforming Solid Oxide Fuel Cells via PDAE-Constrained Dynamic Optimization. *Appl. Energy* **2024**, *360*, 122804. [CrossRef]
13. Yahya, A.; Ferrero, D.; Dhahri, H.; Leone, P.; Slimi, K.; Santarelli, M. Electrochemical Performance of Solid Oxide Fuel Cell: Experimental Study and Calibrated Model. *Energy* **2018**, *142*, 932–943. [CrossRef]
14. Chan, S.H.; Khor, K.A.; Xia, Z.T. A Complete Polarization Model of a Solid Oxide Fuel Cell and Its Sensitivity to the Change of Cell Component Thickness. *J. Power Sources* **2001**, *93*, 130–140. [CrossRef]
15. Biert, L.V.; Godjevac, M.; Visser, K.; Aravind, P. V Dynamic Modelling of a Direct Internal Reforming Solid Oxide Fuel Cell Stack Based on Single Cell Experiments. *Appl. Energy* **2019**, *250*, 976–990. [CrossRef]
16. Srikanth, S.; Heddrich, M.P.; Gupta, S.; Friedrich, K.A. Transient Reversible Solid Oxide Cell Reactor Operation—Experimentally Validated Modeling and Analysis. *Appl. Energy* **2018**, *232*, 473–488. [CrossRef]
17. Min, G.; Park, Y.J.; Hong, J. 1D Thermodynamic Modeling for a Solid Oxide Fuel Cell Stack and Parametric Study for Its Optimal Operating Conditions. *Energy Convers. Manag.* **2020**, *209*, 112614. [CrossRef]
18. Hines, A.L.; Maddox, R.N. *Mass Transfer: Fundamentals and Applications*; Prentice-Hall: Englewood Cliffs, NJ, USA, 1985.
19. Zhu, H.; Kee, R.J. A General Mathematical Model for Analyzing the Performance of Fuel-Cell Membrane-Electrode Assemblies. *J. Power Sources* **2003**, *117*, 61–74. [CrossRef]
20. Poling, B.E.; Prausnitz, J.M.; O'Connell, J.P. *The Properties of Gases and Liquids*, 5th ed.; McGraw-Hill Education: New York, NY, USA, 2001.
21. Hosseinpour, J.; Rizvandi, O.B.; Braun, R.J. Performance Analysis of a MW-Scale Reversible Solid Oxide Cell Energy Storage System Utilizing Steam-Hydrogen Chemistry. *Int. J. Hydrogen Energy* **2025**, *99*, 364–382. [CrossRef]
22. Wang, Q.; Li, L.; Wang, C. Numerical Study of Thermoelectric Characteristics of a Planar Solid Oxide Fuel Cell with Direct Internal Reforming of Methane. *J. Power Sources* **2009**, *186*, 399–407. [CrossRef]
23. Timmermann, H.; Sawady, W.; Reimert, R.; Ivers-tiffée, E. Kinetics of (Reversible) Internal Reforming of Methane in Solid Oxide Fuel Cells under Stationary and APU Conditions. *J. Power Sources* **2010**, *195*, 214–222. [CrossRef]
24. Donazzi, A.; De Pascali, S.; Garavaglia, F.; Bracconi, M. A Quasi 2D Model for the Interpretation of Impedance and Polarization of a Planar Solid Oxide Fuel Cell with Interconnects. *Electrochim. Acta* **2021**, *365*, 137346. [CrossRef]
25. Zhu, H.; Kee, R.J.; Janardhanan, V.M.; Deutschmann, O.; Goodwin, D.G. Modeling Elementary Heterogeneous Chemistry and Electrochemistry in Solid-Oxide Fuel Cells. *J. Electrochem. Soc.* **2005**, *152*, A2427–A2440. [CrossRef]